

Mg²⁺ binding triggers rearrangement of the IM30 ring structure, resulting in augmented exposure of hydrophobic surfaces competent for membrane binding

Received for publication, November 16, 2017, and in revised form, March 20, 2018. Published, Papers in Press, April 4, 2018, DOI 10.1074/jbc.RA117.000991

Jennifer Heidrich^{‡1}, Benedikt Junglas^{‡1}, Natalia Grytsyk[§], Nadja Hellmann[‡], Kristiane Rusitzka[¶], Wolfgang Gebauer[¶], Jürgen Markl[¶], Petra Hellwig[§], and Dirk Schneider^{‡2}

From the [‡]Institut für Pharmazie und Biochemie, Johannes-Gutenberg-Universität Mainz, 55128 Mainz, Germany, [¶]Institut für Molekulare Physiologie, Johannes Gutenberg-Universität Mainz, 55128 Mainz, Germany, and [§]Laboratoire de bioelectrochimie et spectroscopie, UMR 7140, CNRS Université de Strasbourg, 1 rue Blaise Pascal, 67000 Strasbourg, Germany

Edited by Joseph M. Jez

The “inner membrane–associated protein of 30 kDa” (IM30), also known as “vesicle-inducing protein in plastids 1” (Vipp1), is found in the majority of photosynthetic organisms that use oxygen as an energy source, and its occurrence appears to be coupled to the existence of thylakoid membranes in cyanobacteria and chloroplasts. IM30 is most likely involved in thylakoid membrane biogenesis and/or maintenance, and has recently been shown to function as a membrane fusion protein in presence of Mg²⁺. However, the precise role of Mg²⁺ in this process and its impact on the structure and function of IM30 remains unknown. Here, we show that Mg²⁺ binds directly to IM30 with a binding affinity of ~1 mM. Mg²⁺ binding compacts the IM30 structure coupled with an increase in the thermodynamic stability of the proteins’ secondary, tertiary, and quaternary structures. Furthermore, the structural alterations trigger IM30 double ring formation *in vitro* because of increased exposure of hydrophobic surface regions. However, *in vivo* Mg²⁺-triggered exposure of hydrophobic surface regions most likely modulates membrane binding and induces membrane fusion.

An important part of photosynthesis takes place in a specialized structure within chloroplasts and cyanobacteria, the thylakoid membrane (TM)³ system. Although several molecular details of photosynthesis are already understood, it essentially still remains a mystery how TMs are synthesized and maintained in chloroplasts and cyanobacteria. Clearly, TMs develop in the light (1–3), and the TM network is reorganized in response to changing environmental (light) conditions, involving TM assembly and disassembly (1–4). Thus, a mechanism controlling dynamic organization of TMs must exist. In fact,

within the last 15 years, several proteins were discussed to be involved in TM biogenesis, rearrangement, and maintenance, including the “inner membrane–associated protein of 30 kDa” (IM30).

IM30 was initially discovered in chloroplasts of *Pisum sativum*, where it was found to localize at both the inner envelope membrane and TMs (5). Most likely, IM30 has evolved from the “phage shock protein A” (PspA) in a cyanobacterial ancestor as a result of a gene duplication event (6). PspA is a 25-kDa protein involved in bacterial stress response (7, 8) and solely encoded in bacteria. Whereas in chloroplasts exclusively IM30 is present, cyanobacterial genomes code for both proteins (8).

Because of their common origin, IM30 and PspA share several structural and functional similarities: Both proteins are peripheral membrane-binding proteins (5, 8–11) that have a conserved secondary structure, which is mainly α -helical, interrupted by small loop regions (11–14). The most obvious structural difference between PspA and IM30 monomers is the existence of an extra α -helix at the IM30 C terminus (6, 14). Both PspA and IM30 form large ring assemblies with molecular masses >1 MDa (11–13, 15). However, whereas PspA appears to form one type of ring with a well-defined size and a 9-fold internal symmetry (13), IM30 forms diverse oligomeric rings with varying rotational symmetries of at least 7–22 (11, 12). We were recently able to generate a 3D surface representation of several IM30 rings, and based on these structures and mutant analyses we could show that the ring top and bottom clearly differ, and the IM30-specific C terminus, for example, is located exclusively at the ring top side (16). However, because a detailed structure of full-length IM30 or PspA is not available yet, it is still unclear how the monomers precisely pack inside these rings.

Although the exact physiological function of IM30 still is under debate, because of its dual localization at the chloroplast inner envelope membrane plus at the TM, it has early been assumed that the protein is involved in TM biogenesis in chloroplasts (5). Depletion of IM30 in *Arabidopsis thaliana* (9, 17) and the cyanobacterium *Synechocystis* sp. PCC 6803 (6, 18) resulted in a reduced and disordered thylakoid structure and in an overall disturbed photosynthesis efficiency, which supports the assumption of an involvement in TM biogenesis and maintenance. In the last two decades, various IM30 functions have

This work was funded by the Max-Planck Graduate Center at the Max Planck Institutes and the University of Mainz (to J. H., B. J., and D. S.) and iCFC Strasbourg (to N. G.). The authors declare that they have no conflicts of interest with the contents of this article.

This article contains Figs. S1–S8.

¹ These authors contributed equally to this work.

² To whom correspondence should be addressed: Johann-Joachim-Becher-Weg 30, 55128 Mainz, Germany. Tel.: 49-6131-39-25833; Fax: 49-6131-39-25348; E-mail: Dirk.Schneider@uni-mainz.de.

³ The abbreviations used are: TM, thylakoid membrane; ITC, isothermal titration calorimetry; ANS, 8-anilino-1-naphthalene-1-sulfonic acid; TEM, transmission EM; Rubisco, ribulose-1,5-bisphosphate carboxylase-oxygenase; DOPG, 1,2-dioleoyl-sn-glycero-3-phospho-(1'-rac-glycerol).

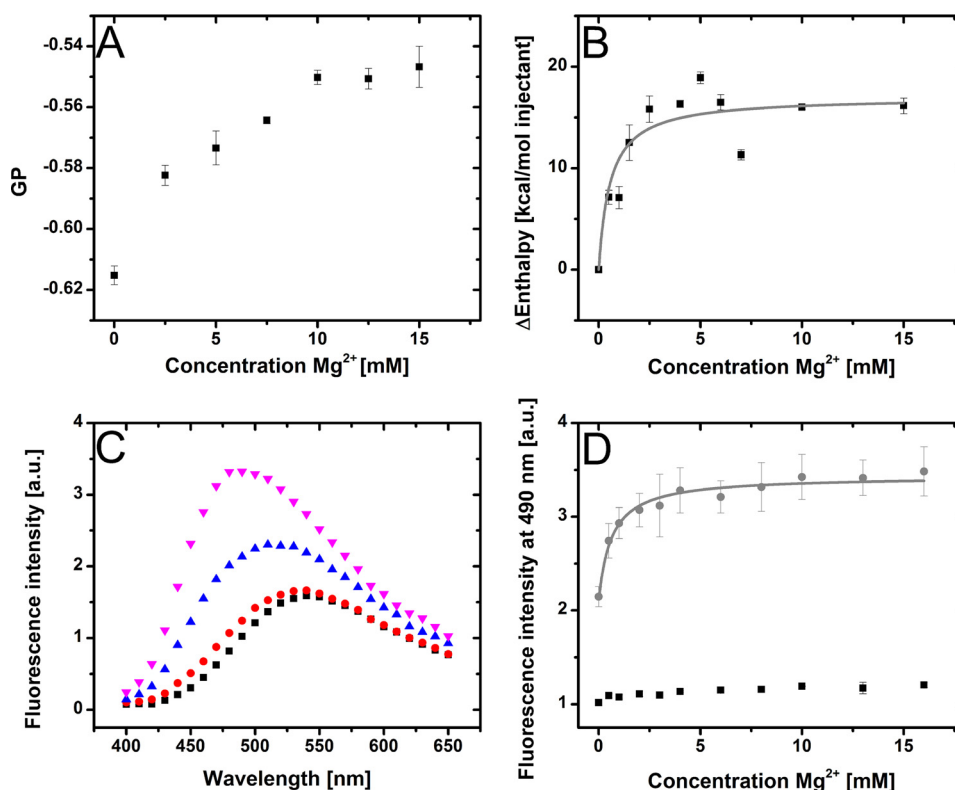


Figure 1. Mg²⁺ binding to IM30 alters the protein surface hydrophobicity. A, generalized polarization (GP) of Laurdan fluorescence measured with DOPG liposomes in presence of increasing Mg²⁺ concentrations. Mg²⁺ addition increases the GP value in a concentration-dependent manner. Error bars represent S.D. ($n = 3$). B, binding of Mg²⁺ to IM30 (black squares) is coupled to a positive enthalpy change. The ITC data were fitted with a standard one-site binding model (gray line). Error bars represent S.D. ($n = 3$). C, fluorescence spectra of ANS in presence of IM30 ± Mg²⁺ (blue triangles, IM30 WT, 0 mM Mg²⁺; pink triangles, IM30 WT, 16 mM Mg²⁺; black squares, IM30-X, 0 mM Mg²⁺; red circles, IM30-X, 16 mM Mg²⁺). Binding of Mg²⁺ to IM30 causes an intensity increase and a blue shift of the ANS fluorescence peak. Spectra were averaged from nine samples. D, ANS fluorescence intensities at 490 nm in presence of increasing Mg²⁺ concentrations (black squares, IM30-X; gray circles, IM30 WT). Error bars represent S.D. ($n = 9$, IM30 WT; $n = 3$, IM30-X).

been proposed, including lipid and/or protein transport, protein complex formation, organization of thylakoid centers, the formation of cytoskeleton-like structures, and membrane protection (for a recent review see Ref. 19). Because under defined experimental conditions structures reminiscent of budding vesicles were observed at the inner chloroplast envelope membrane in IM30-depleted *A. thaliana* chloroplasts (9), renaming the protein to “vesicle inducing protein in plastids 1, Vipp1” has been suggested. However, subsequent indications for an involvement in vesicle formation are lacking. Rather, we recently established that IM30 can trigger membrane fusion (10), an activity that explains several of the observations made before with IM30-depleted cyanobacteria and chloroplasts. Importantly, for IM30-induced membrane fusion, the presence of Mg²⁺ is absolutely required (10). This was an important observation, as Mg²⁺ is globally involved in regulating light-dependent processes in chloroplasts and appears to regulate the activity of several chloroplast proteins (20–23). However, does IM30 simply act as “glue” between the membrane and IM30, or does Mg²⁺ bind to IM30 and induce structural rearrangements necessary for membrane binding and/or fusion? Thus, does Mg²⁺ directly activate IM30?

Here we show that Mg²⁺ binds to IM30, and Mg²⁺ binding stabilizes the IM30 secondary as well as the tertiary and quaternary structure. The Mg²⁺ binding affinity is about 1 mM, a value that would allow “activation” of IM30 and controlling its activ-

ity by the changes in the Mg²⁺ concentration observed *in vivo*. Mg²⁺ binding induces reorganization of the protein structure resulting in increased exposure of hydrophobic surfaces. *In vitro*, this results in ring clustering and double ring formation. However, *in vivo* exposure of increased hydrophobic surface regions most likely modulates membrane binding and induces membrane fusion.

Results

Mg²⁺ binding changes the hydrophobicity of the IM30 ring surface

Recently, we have demonstrated that IM30 mediates membrane fusion in presence of Mg²⁺ (10). However, the exact role of Mg²⁺ in the fusion process is still enigmatic, and either (i) Mg²⁺ binding to IM30 results in a rearrangement of the IM30 structure that, in the end, triggers membrane fusion or (ii) alternatively, Mg²⁺ serves as a bridging ion that, glue-like, connects IM30 with the membrane.

It is well-established that Mg²⁺ binds to negatively charged lipid bilayers, for example, those formed of 1,2-dioleoyl-sn-glycero-3-phospho-(1'-rac-glycerol) (DOPG) (24). We could verify this via addition of Mg²⁺ to DOPG liposomes containing the fluorescence probe Laurdan, which senses changes in the polarity of the lipid head-group region (25) (Fig. 1A). Thus, Mg²⁺ binding to negatively charged membrane surfaces could

Mg²⁺ binding triggers rearrangement of the IM30 ring

indeed mediate membrane attachment of IM30. However, this does not exclude that Mg²⁺ also directly binds to IM30 and that this is (additionally) needed for membrane fusion.

To follow binding of Mg²⁺ to IM30, we at first employed isothermal titration calorimetry (ITC). We had to use a reverse ITC protocol because injection of highly concentrated Mg²⁺ solutions into an IM30 protein solution, as would be necessary for “normal” ITC experiments, caused a very high heat of dilution (data not shown), masking the signal for the IM30–Mg²⁺ interaction. Although even with the reverse ITC setup the heat of dilution background for Mg²⁺ was very high (Fig. S1), a direct interaction between Mg²⁺ and IM30 was observed (Fig. 1B). To estimate the binding affinity, a simple hyperbolic binding model was fitted to the data, revealing a K_d of 0.6 ± 0.3 mM (Fig. 1B). It should be noted that data analysis was limited to the concentration range up to 15 mM Mg²⁺ because of the large heat of dilution at higher Mg²⁺ concentrations.

Whereas binding of divalent cations, such as Mg²⁺, typically is a result of electrostatic interactions, which are characterized by negative enthalpy changes, binding of Mg²⁺ to IM30 resulted in a positive ΔH of up to 20 kcal/mol, and thus appears to be entropically driven. For example, this could be explained by a Mg²⁺-induced rearrangement of the IM30 structure that involves an altered protein surface chemistry, resulting in the release of water molecules, or by an involvement of proton transfer between protein and buffer, which can severely affect observed binding enthalpies (26).

To tackle these possibilities, we analyzed whether the surface properties of IM30 change after addition of increasing Mg²⁺ concentrations. The fluorescence dye 8-anilino-1-naphthalene-sulfonic acid (ANS) binds to protein surfaces via hydrophobic interactions to exposed hydrophobic patches as well as via salt bridge formation between the dye's sulfonate group and positively charged amino acid side chains (27). Binding of the dye to a protein is observed as an increase in the ANS fluorescence intensity coupled with a blue shift of the fluorescence emission maximum (28). As can be seen in Fig. 1C, addition of Mg²⁺ led to increased fluorescence intensities and a blue shift of the fluorescence emission maximum from 525 nm to 490 nm, demonstrating increased binding of ANS to the protein surface in presence of increasing Mg²⁺ concentrations. Importantly, significant differences in the relative ANS fluorescence were not observed in the absence of protein, clearly indicating that Mg²⁺ does not directly influence the ANS fluorescence (data not shown). Furthermore, the observed effect is Mg²⁺ specific, because increasing the ionic strength by addition of NaCl did not significantly affect ANS binding (Fig. S2). Most likely, the observed changes in the fluorescence were caused by increased ANS binding to hydrophobic patches on the protein surface, because ANS binding mediated by ionic interactions is dramatically weaker than binding via hydrophobic interactions (27). Thus, the above-described observations strongly suggested that Mg²⁺ binding to IM30 induces structural rearrangements, which result in increased exposure of hydrophobic surface regions. The determined increase in the fluorescence intensity with increasing Mg²⁺ concentrations (Fig. 1D) could be well-described by a hyperbolic function, yielding a dissociation con-

stant K_d of 0.6 ± 1.9 mM, a value in good agreement with the K_d value determined before in the ITC experiments (Fig. 1B).

To further support the assumption that Mg²⁺ binding alters the IM30 structure, we next measured ANS fluorescence at increasing Mg²⁺ concentrations, using chemically cross-linked IM30 rings (IM30-X). We anticipated that cross-linking the protein in absence of Mg²⁺ would stabilize the Mg²⁺ free ring conformation and would abolish (or at least hinder) Mg²⁺ binding and/or structural rearrangements occurring upon Mg²⁺ addition. Indeed, the ANS fluorescence spectra did not change upon addition of Mg²⁺ to IM30-X (Fig. 1, C and D), and thus, cross-linking clearly inhibits ANS binding. It is worth noting that IM30-X and WT IM30 have identical secondary and quaternary structures in absence of Mg²⁺ (Fig. S3A), and neither is altered significantly by addition of Mg²⁺ to IM30-X (Fig. S3B). It is significant that we cannot completely rule out that Mg²⁺ still binds to the cross-linked protein. Although in ITC measurements the titration of Mg²⁺ into an IM30-X solution led to reaction heats undistinguishable from the control (data not shown), this does not completely rule out Mg²⁺ binding because of the large heat of dilution (control).

Together, the observations described strongly suggest that Mg²⁺ directly binds to IM30 with a K_d of about 1 mM. Mg²⁺ binding involves structural rearrangements of flexible and solvent accessible domains, resulting in increased exposure of hydrophobic regions.

Mg²⁺ binding results in deprotonation of carboxyl groups

Exposure of hydrophobic surface regions is typically accompanied by increased ordering of surrounding water molecules and with a decrease of entropy, which, however, seems to contradict the results of the ITC measurement (Fig. 1B). The increase in entropy deduced from the ITC measurements might be because of deprotonation events coupled with Mg²⁺ binding and/or subsequent structural rearrangement of IM30, however. Depending on the pH and buffer conditions, the influence of the protonation enthalpy on observed binding enthalpies can be significant. Because the entropy is calculated from the difference between binding enthalpy and free energy obtained from the binding constant, a shift in the experimentally determined binding enthalpy because of protonation of the buffer would lead to an incorrect value for the binding entropy. Thus, in case of proton transfer the here calculated binding enthalpy $\Delta H_{\text{binding}}$ would not represent the intrinsic binding enthalpy.

In fact, difference absorption FTIR spectroscopy of IM30 in absence and presence of Mg²⁺ indicated that Mg²⁺ binding to IM30 involves deprotonation events. The absorption in the 1720 cm⁻¹ region (Fig. 2), which monitors COOH stretching vibrations, is decreased in the presence of Mg²⁺, which strongly indicates deprotonation of carboxyl groups, most likely from Glu and/or Asp side chains (29). Furthermore, the absorption of the IM30 amide I band (~1650 cm⁻¹) is increased in presence of Mg²⁺ (Fig. 2). This difference, which is even more pronounced at higher Mg²⁺ concentrations (Fig. S4A), clearly suggests a Mg²⁺-induced rearrangement of the peptide backbone (amide I band) and thus, the secondary structure (30).

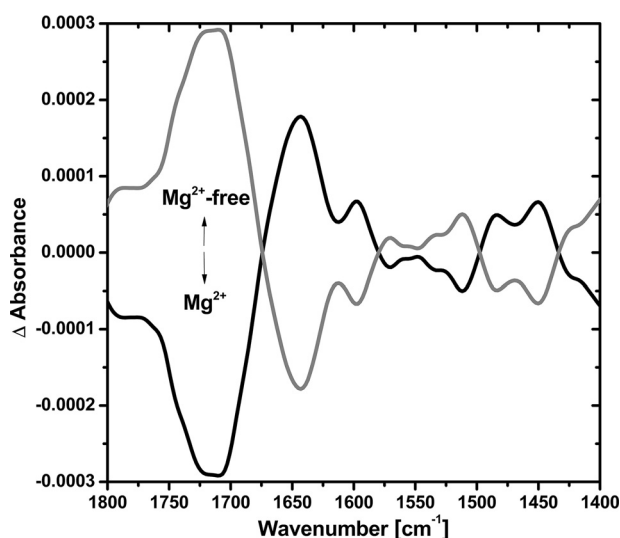


Figure 2. FTIR difference absorbance spectra of IM30 \pm Mg²⁺. Shown are the FTIR difference absorbance spectra of IM30 in absence of 10 mM Mg²⁺ (gray line, 20 mM HEPES – (20 mM HEPES + 10 mM Mg²⁺)) and in presence of 10 mM Mg²⁺ (black line, (20 mM HEPES + 10 mM Mg²⁺) – 20 mM HEPES). Significant changes can be observed in the range of 1400–1800 cm^{–1}. The data show increased absorbance of the amide I band and decreased absorbance in the 1720 cm^{–1} region in presence of 10 mM Mg²⁺.

Mg²⁺ binding stabilizes IM30

As IM30 is a predominantly α -helical protein (11, 12), we next used CD spectroscopy to further examine the Mg²⁺-induced structural alterations indicated in our FTIR measurements. Because exposure of hydrophobic patches should destabilize the protein, the stability of IM30 against urea-induced denaturation was investigated. The CD spectrum of IM30 in absence of urea suggests that the protein has a largely α -helical structure, regardless of the Mg²⁺ concentration (Fig. 3A), which is in line with previous results (11). However, in presence of Mg²⁺, the denaturation curve transition point ($D_{1/2}$) is clearly shifted to higher urea concentrations (Fig. 3, C and D and Fig. S5C), and the slope of the curve is increased compared with the protein in absence of Mg²⁺ (Fig. 3C). Although the original level of secondary structure could be regained after removal of urea (Fig. S5B), the denaturation and renaturation curves do not overlap. Thus, the system shows hysteresis (Fig. S5A), and therefore we refrained from calculating ΔG values.

Whereas the above-described experiments suggest that Mg²⁺ binding stabilizes the IM30 secondary structure, the molecular details of this stabilization were unclear. However, we speculated that a more tightly packed IM30 ring structure eventually stabilizes the secondary structure by reducing the accessibility of the protein core for the denaturant, thereby increasing the apparent thermodynamic stability. This assumption was supported by the notion that an increased slope of the denaturation curve as observed in presence of Mg²⁺ could indicate a reduced solvent accessible surface area (31). In fact, a closer inspection of the CD spectra in absence and presence of Mg²⁺ further supports the assumption of a more compact structure. The ratio of the CD signal at 222 nm and 208 nm is a measure for coiled coil-type interactions of α -helices (32), and with a 222/208 ratio of >1.0 , coiled coil-type interactions are clearly involved in formation and stabilization of the IM30

structure (Fig. 3B), in line with previous reports (33). Importantly, the 222/208 ratio increases in presence of Mg²⁺, indicating increased formation of intramolecular and/or intermolecular helix–helix interactions (Fig. 3B).

To better understand the impact Mg²⁺ binding has on the IM30 tertiary and quaternary structure, we next determined the accessibility of Trp-71, which is located in Helix 2 (14), for the fluorescence quencher acrylamide. The Trp-71 fluorescence was quenched successively with increasing acrylamide concentration, with a higher slope, denoted as Stern–Volmer constant, in absence of Mg²⁺ (Fig. 3E). The Stern–Volmer constant changed from 3.24 M^{–1} in absence of Mg²⁺ to 2.46 M^{–1} in presence of Mg²⁺ (Fig. 3E), and is in the same range as observed in previous studies analyzing proteins with buried Trps (34). Thus, the Trp fluorescence quenching measurements indicate that Trp-71 is already buried within the IM30 structure in absence of Mg²⁺. However, in presence of Mg²⁺, the accessibility of Trp-71 for acrylamide is decreased (Fig. 3E), and thus the Mg²⁺-induced changes in the IM30 tertiary and/or quaternary structure further shield Trp-71 within the oligomeric IM30 structure.

Mg²⁺ binding protects the IM30 C-terminal domain against proteolytic cleavage

To further elucidate the impact Mg²⁺ binding has on the IM30 structure, IM30 was digested by trypsin in presence and absence of Mg²⁺, as an altered IM30 structure could result in altered proteolytic stability of the protein. When analyzed via SDS-PAGE, the full-length protein started to disappear already 2 min after addition of trypsin and a weak band with an apparent molecular mass of ~ 40 kDa appeared instead, which remained stable for about 40 min (Fig. 4A). In presence of Mg²⁺, the original band remained visible significantly longer and the 40-kDa band was hardly detectable (Fig. 4A). The small fragment removed in absence of Mg²⁺ contains the IM30 C terminus, as in the corresponding Western blot, the 40-kDa band was not detected by an antibody specifically recognizing the IM30 C-terminal domain (Fig. 4B). It is noteworthy that a direct impact of Mg²⁺ on the trypsin activity was excluded (Fig. S6). Thus, in presence of Mg²⁺ the IM30 structure is altered and the C terminus has a decreased trypsin accessibility, *i.e.* is differently structured and/or located.

All results obtained thus far clearly indicate that Mg²⁺ binding induces structural rearrangements, and the proteolysis data suggest a different structure and/or position of the IM30 C terminus in presence of Mg²⁺. Consequently, we next investigated the spatial proximity of IM30 C termini in presence and absence of Mg²⁺. FRET measurements were performed using IM30 rings composed of IM30 monomers that are labeled at their respective C terminus with CFP or Venus, a YFP variant. Importantly, proper ring formation of both mutants was demonstrated via SEM and transmission EM (TEM) (Fig. S8), and we have just recently demonstrated that the IM30 *in vivo* activity is not compromised by the fusion tag (35).

When differently labeled IM30 rings were mixed in a 1:1 ratio, the ratiometric FRET efficiency E_{rat} increased continuously from initially ~ 0.15 up to ~ 0.4 , reached at Mg²⁺ concentrations >20 mM (Fig. 5A). Additionally, the time required to

Mg²⁺ binding triggers rearrangement of the IM30 ring

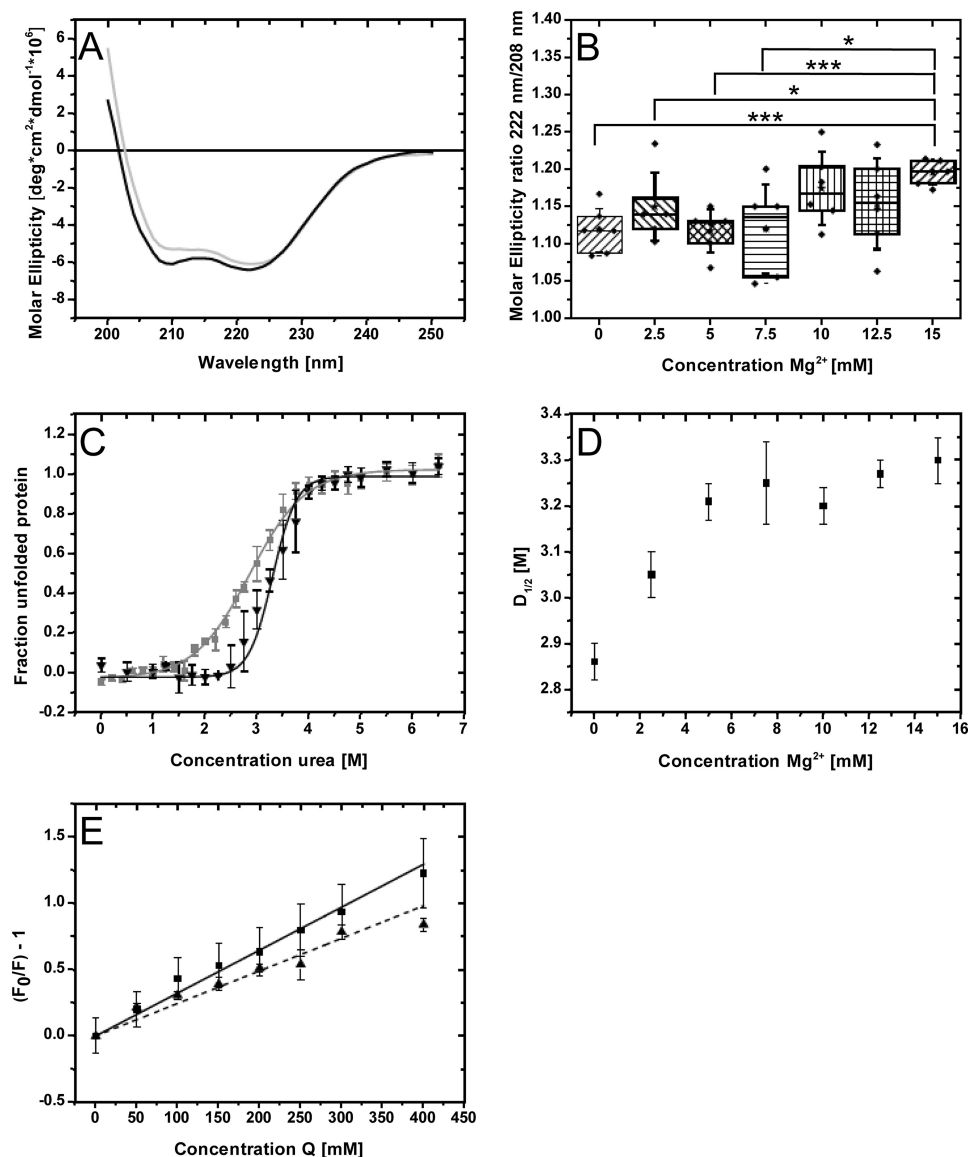


Figure 3. Mg²⁺ binding affects the secondary/tertiary/quaternary structure and stability of IM30. A, CD spectra of IM30 in absence (black line) and in presence of 15 mM Mg²⁺ (gray line). The 208 nm peak amplitude is decreased in presence of Mg²⁺, indicating a change in protein structure. Spectra were averaged from three samples. B, box plots of the 222/208 ratio at increasing Mg²⁺ concentrations. The boxes represent the lower and upper quartile relative to the mean value, whiskers represent the S.D. The arithmetic mean is marked by an asterisk ($n = 6-7$). The 222/208 ratio increases with increasing Mg²⁺ concentration, indicating increased formation of coiled coil-type structures. Significance levels: *, $p \leq 0.05$; **, $p \leq 0.01$; ***, $p \leq 0.001$. C, urea denaturation of IM30 in absence (gray squares) and presence of 15 mM Mg²⁺ (black triangles). The denaturation curves show a stability increase as a shift of the inflection point to a higher urea concentration in presence of 15 mM Mg²⁺. The curves show averaged data of three independent experiments. Lines, fit, based on a Boltzmann function. Error bars represent Gauss errors of three samples ($n = 3$). D, $D_{1/2}$ values of IM30 calculated from urea denaturation curves gained in presence of increasing Mg²⁺ concentrations (black squares). The stability of the secondary structure increases with increasing Mg²⁺ concentration for both values. Error bars represent error for $D_{1/2}$ of the least square nonlinear fit of three averaged denaturation curves. E, Stern-Volmer plot of IM30 Trp fluorescence quenching by acrylamide in presence (black triangles) and absence (black squares) of 15 mM Mg²⁺. The slope of the linear regression decreases in presence of 15 mM Mg²⁺. The K_{SV} for the control is $3.24 \pm 0.12 \text{ M}^{-1}$, and $2.46 \pm 0.14 \text{ M}^{-1}$ in presence of Mg²⁺. Thus, Trp is more buried within the IM30 ring structure in presence of Mg²⁺. Error bars, S.D. of three samples ($n = 3$).

achieve a stable E_{rat} value was altered when Mg²⁺ was present, whereas in absence of Mg²⁺ it took about 7 h to reach the final value; in presence of 7.5 mM Mg²⁺ a constant value was reached already after ~ 2 h (Fig. 5B).

The observed increasing FRET efficiencies could originate from (i) Mg²⁺ binding enforcing IM30 monomers or lower ordered oligomeric structures to form high oligomeric ring structures, (ii) individual monomers exchanging more easily between two rings upon Mg²⁺ binding, or (iii) a dye-dye cross-talk between different IM30 rings, e.g. because of ring-ring

interactions. Based on previous analyses we ruled out the possibility that a significant fraction of IM30 is monomeric or present as low-oligomeric forms (36). To be able to tackle option (ii), we next determined the maximal E_{rat} value by measuring the fluorescence emission of IM30 rings carrying both IM30-CFP and IM30-Venus monomers in an about 1:1 ratio. Using these dual-labeled IM30 rings, the maximum E_{rat} value was calculated to be 0.54 ± 0.01 (data not shown). This value was not reached by far after mixing single-labeled IM30 rings, even after incubation for 15 h, and thus we excluded a substantial

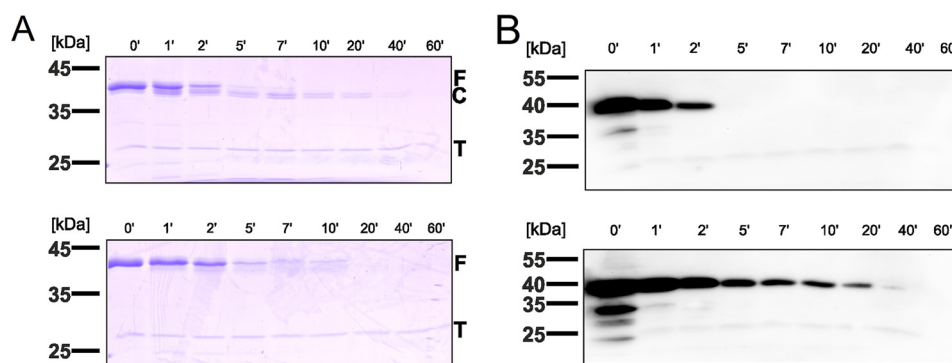


Figure 4. Mg²⁺ binding affects tryptic digestion of IM30. A, SDS-PAGE following trypsin digestion of IM30 in absence (top) and presence of 10 mM Mg²⁺ (bottom). F marks the full-length protein, C the protein core fragment after cleavage of an easily accessible fragment, and T trypsin. In absence of Mg²⁺, a small fragment is cleaved rapidly, whereas a stable core fragment is detectable for at least 20 min. The full-length protein is only detectable for 2 min. In presence of Mg²⁺, the full-length protein can be detected for at least 10 min. B, immunoblot of IM30 after trypsin digestion in absence (top) and presence of 10 mM Mg²⁺ (bottom) using an antibody directed against the IM30 C terminus. In absence of Mg²⁺, the C-terminal domain is detectable for 2 min, whereas it is detectable for at least 20 min in presence of Mg²⁺. Therefore, Mg²⁺ binding protects the C-terminal domain against tryptic digestion.

monomer exchange between rings. Thus, a ring–ring interaction (iii), resulting in increased FRET, seemed to be most likely.

In fact, TEM of negatively stained IM30 indeed indicated an increased formation of IM30 double rings and a small number of rod structures in presence of Mg²⁺ (Fig. 5C). Such aggregates can also be observed in absence of Mg²⁺, but to a much lower extent (11). When analyzed more quantitatively via static light scattering, the average IM30 particle size increased with increasing Mg²⁺ concentrations (Fig. 5D), supporting the assumption that Mg²⁺-induced ring stacking is the major cause of the increasing E_{rat} value in presence of Mg²⁺. Importantly, we can rule out the possibility that IM30 ring stacking is caused by an unspecific effect of increased ionic strength, because we did not observe an increased particle size when we increased the cation concentration by equivalent levels of Na⁺ (Fig. S7). Thus, the structural rearrangements observed upon addition of Mg²⁺ result in ring stacking, which leads to an overall shielding of the C terminus.

Discussion

Recently, we have identified Mg²⁺ as an important cofactor involved in IM30-mediated membrane fusion (10). However, its exact mode of action was unclear and we hypothesized that Mg²⁺ either acts as a bridging ion, mediating interaction of the protein with negatively charged membrane surfaces, or that Mg²⁺ directly binds to IM30, resulting in structural rearrangement and finally in formation of fusion-competent IM30 rings. Although Mg²⁺ clearly binds to negatively charged membrane surfaces (24) (Fig. 1A), and could thus act as a bridging ion, such a glue is not required, as IM30 rings already bind to negatively charged membrane surfaces in absence of Mg²⁺ (10, 36). However, the results presented here suggest that Mg²⁺ directly binds to IM30 rings resulting in structural rearrangements, coupled with an increased exposure of hydrophobic surface regions, finally resulting in ring stacking, at least *in vitro*. Albeit we are not yet able to pinpoint the exact Mg²⁺-binding site(s) at IM30, the FTIR data suggest that Asp and/or Glu side chains are involved in Mg²⁺ binding (Fig. 2). In fact, Mg²⁺ favors an octahedral coordination sphere with strong oxygen containing Lewis bases, such as carboxyl groups (37).

In the past, the activity of several prokaryotic and eukaryotic proteins has been demonstrated to depend on Mg²⁺ (38–41). Most importantly, regulation of enzymatic activity via Mg²⁺ is well-described in chloroplasts, and, for example, the activities of the CO₂-fixing enzyme Rubisco (42), fructose-1,6-bisphosphatase (43), and sedoheptulose-1,7-bisphosphatase (43) are regulated by Mg²⁺. Mg²⁺ is the most abundant metal ion in the TM lumen and in the chloroplast cytosol (20, 23), and the concentration of free Mg²⁺ in chloroplasts is estimated to be in the range of 0.4 to 120 mM for different plant tissues and compartments (reviewed in Ref. 44). However, the spatiotemporal Mg²⁺ concentration in the chloroplast stroma depends on the environmental light conditions, as light exposure induces an increase in the stromal Mg²⁺ concentration (21, 45–47) because of a Mg²⁺ release from the TM lumen (22). This change in the stromal Mg²⁺ concentration is key for regulation of above-described enzymatic activities. Thus, it is not far-fetched to assume that Mg²⁺ plays a role also in regulation of TM biogenesis, maintenance, and dynamics, because TMs develop and remodel in the light (1–3).

Binding of Mg²⁺ to IM30 could be key for TM maintenance and dynamics because the here-determined K_d of ~1 mM lies in the transition range of the stromal Mg²⁺ concentration. Likely, a light-induced increase in the Mg²⁺ concentration within the chloroplast stroma and the cyanobacterial cytoplasm activates the IM30 inherent fusion activity. Mg²⁺ binding to IM30 induces a rearrangement of the IM30 structure involving formation of new or constriction of existing helix–helix interactions (Fig. 3B), leading to a more tightly packed structure with increased thermodynamic stability plus an exposure of extra hydrophobic surface regions. As we observed increased double ring formation in presence of Mg²⁺ (Fig. 5), it is reasonable to assume that, in absence of a membrane, the newly exposed hydrophobic surface triggers homodimerization of IM30 rings. In principle, such double rings could form via head-to-head, tail-to-tail, or head-to-tail interaction of two rings. However, a head-to-tail interaction would ultimately result in formation of longer IM30 rods, which was observed only in a few cases here. Furthermore, as the Förster distance of the CFP/YFP pair is in the range of 50 Å (48) and as a single ring has a height of about

Mg^{2+} binding triggers rearrangement of the IM30 ring

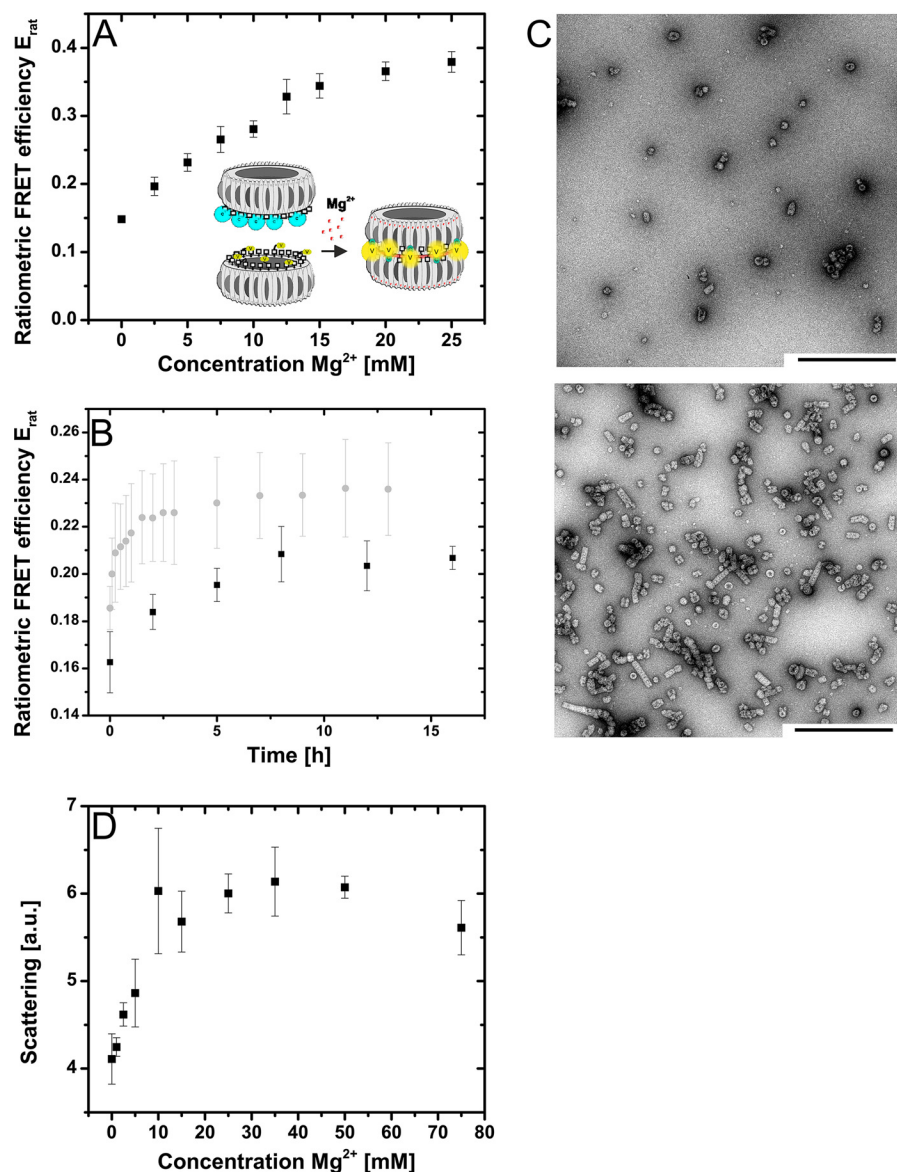


Figure 5. Mg^{2+} triggers stacking of IM30 rings. A, FRET between IM30 CFP and IM30 Venus is caused by stacking of IM30 rings in presence of Mg^{2+} (see text for details). FRET between IM30 CFP and IM30 Venus increases with increasing Mg^{2+} concentrations. Error bars represent S.D. of three samples ($n = 3$). B, FRET between IM30 CFP and IM30 Venus in presence (gray circles) and absence (black squares) of 7.5 mM Mg^{2+} followed over time. The plateau is higher and is reached faster in presence of Mg^{2+} . Error bars represent S.D. of three samples ($n = 3$). C, negative stain TEM of IM30 (6.3 μ m) in absence (top) and presence (bottom) of 15 mM Mg^{2+} . Both samples were from the identical protein stock solution. The number of double rings and rod structures increases in presence of Mg^{2+} . Apparently, the amount of protein found on the grid is also increased in presence of Mg^{2+} , which might be caused by better binding to the grid as a result of the altered protein surface in presence of Mg^{2+} . Scale bars = 500 nm. D, light scattering of IM30 at increasing Mg^{2+} concentrations. Scattering increases with increasing Mg^{2+} concentrations, caused by an increased particle size. Error bars represent S.D. of three samples ($n = 3$).

140 Å (*i.e.* a double ring has a height of ~280 Å) (16), solely formation of double rings via the ring top surfaces containing the C termini (that carry CFP/YFP) satisfactorily explains the observed increase in the FRET signals upon Mg^{2+} -induced double ring formation (Fig. 5A). Thus, IM30 double rings likely form via the upper ring surface that contains the C-terminal tail, and this C-terminal IM30 tail (Helix 7) is then buried within the ring–ring interface, as indicated by the decreased protease sensitivity. However, *in vivo*, in presence of a cellular membrane, the hydrophobic patches of IM30 rings likely interact with the membrane, bringing the C terminus in contact with the membrane surface. Indeed, the isolated IM30 C terminus forms an amphipathic α -helix that can interact with mem-

branes (49). Actually, the K_d for the IM30–membrane interaction was recently determined to be in the micromolar range already in the absence of Mg^{2+} (36), indicating that a significant amount of IM30 rings likely are already membrane bound in absence of Mg^{2+} . Thus, increasing the Mg^{2+} availability in the stroma/cytosol on one hand might result in an increased membrane-binding affinity of soluble IM30 rings because of the increased hydrophobicity of the protein surface, but could also alter the structure of membrane-attached IM30 rings. Membrane fusion involves the ability to connect two membrane layers, and thus Mg^{2+} activation of IM30 rings has to involve formation of IM30 rings exposing hydrophobic regions at both the ring top and bottom (16). Although

we show an increased hydrophobic surface on the top side of IM30 rings, likely promoting membrane interactions, our observations do not exclude that the ring bottom can also interact with membranes after IM30 activation, as suggested recently (16).

Experimental procedures

Cloning, expression, and purification of IM30

Construction of the pRSET-His-IM30 plasmid for expression of His-tagged IM30 is described in detail in Ref. 18. The plasmid for expression of the His-IM30-CFP mutant was constructed using the pRSET-His-IM30 expression plasmid (11), which contains the His-tagged IM30 coding sequence of *Synechocystis* sp. PCC 6803. pRSET-His-IM30 as well as pRSET-CFP, containing the sequence for the cyan fluorescent protein as described in Ref. 50 with the two modifications R27K and H232L, were restriction digested by BamHI and XbaI. The respective fragments were isolated from a 1% agarose gel and ligated by T4 ligase, resulting in the plasmid pRSET-His-IM30-CFP.

The plasmid for expression of the His-tagged IM30-Venus mutant was generated using the pRSET-His-IM30-CFP expression plasmid as a template. From a pVenus plasmid (51), the *venus* gene was amplified using the primers 5'-TAA GCA GGA TCC GTG AGC AAG GGC GAG GAC-3' and 5'-TGC TTA GAA TTC TTA CTT GTA CAG CTC GTC CAT GCC-3'. Via the primers, a BamHI restriction site was introduced at the 5' end and an *EcoRI* restriction site at the 3' end (underlined). Insert and template were restriction digested with BamHI and *EcoRI* and ligated using T4 ligase. All enzymes were from New England Biolabs (Frankfurt am Main, Germany).

All proteins were heterologously expressed in *Escherichia coli* BL21 (DE3) cells and purified with a Ni-NTA-Agarose Column (Qiagen, Hilden, Germany), as described in Refs. 10 and 36. Purified proteins were extensively dialyzed against 20 mM HEPES buffer, pH 7.6, and the purity of the proteins was analyzed on 14% SDS-polyacrylamide gels. Protein concentration was determined using a Bradford assay. For the labeled mutants, SDS-polyacrylamide gels calibrated with BSA standards were densitometrically evaluated to estimate the protein concentration.

Protein cross-linking

IM30 was cross-linked with glutaraldehyde (Sigma-Aldrich). This bifunctional cross-linker reacts with functional groups such as amines, thiols, phenols, and imidazoles (52), thereby decreasing the structural flexibility and dissociation/oligomerization of proteins (53).

IM30 with concentrations between 3 and 10 μ M (in 20 mM HEPES, pH 7.6) were incubated with 5 mM glutaraldehyde for 5 min at 37 °C. The reaction was stopped by adding Tris-HCl, pH 8.5 to a final concentration of 50 mM. The reaction solution was extensively dialyzed against 20 mM HEPES buffer, pH 7.6. A nearly quantitative cross-linking of IM30 was confirmed on 14% SDS-polyacrylamide gels.

Liposome preparation

DOPG (Avanti Polar Lipids, Inc., Alabaster, AL) dissolved in chloroform was mixed with Laurdan (6-dodecanoyl-*N,N*-dimethyl-2-naphthylamine) (Fluka Analytical, Seelze, Germany) dissolved in chloroform in a molar ratio of 1:500 (Laurdan: lipid). The mixture was dried under a stream of nitrogen. To remove traces of chloroform, the mixture was desiccated under vacuum overnight. Lipids were hydrated in HEPES buffer with vigorous stirring to yield multilamellar liposomes. Unilamellar liposomes were formed by five freeze-thaw cycles.

Fluorescence measurements

If not mentioned otherwise, all fluorescence measurements were performed on a FluoroMax-4 fluorimeter (Horiba Scientific, Kyoto, Japan) with an integration time of 0.1 s at 25 °C.

For the ANS fluorescence measurements, 1 μ M IM30 or cross-linked IM30 (IM30-X) was mixed with 7.5 μ M ANS (Sigma-Aldrich) in 20 mM HEPES buffer, pH 7.6, respectively, and incubated in the dark for 15 min at room temperature. Then, increasing amounts of MgCl₂ in a fixed buffer volume were added to reach a final sample volume of 200 μ l. As a control, samples containing NaCl instead of MgCl₂ with the same equivalent concentration of cations were prepared. The samples were incubated at room temperature in the dark for another 30 min. The total concentration of Mg²⁺ ranged from 0 to 128 mM. The excitation wavelength was 370 nm (slit width 4 nm), the emission wavelength ranged from 400 to 650 nm (slit width 4 nm). Fluorescence intensities of at least three independent measurements were averaged and plotted against increasing ionic strength of the monitored cation species. The dissociation constant K_d of Mg²⁺ binding to IM30 was obtained by fitting the following hyperbolic binding function to the data:

$$F = F_{\min} + \frac{\Delta F}{1 + \frac{K_d}{x}} \quad (\text{Eq. 1})$$

Here, F is the measured fluorescence intensity, F_{\min} is the fluorescence intensity in absence of Mg²⁺, ΔF is the change in fluorescence intensity because of Mg²⁺ binding, and x is the Mg²⁺ concentration. The fit was performed with the nonlinear regression tool implemented in OriginPro 8.6.0.

Laurdan fluorescence measurements

DOPG liposomes (100 μ M lipid) in 20 mM HEPES buffer, pH 7.6, were incubated with increasing concentrations of Mg²⁺ (0–15 mM) in separate samples at room temperature for 30 min. Fluorescence intensities were measured with an FLUOstar Omega plate reader (BMG Labtech, Ortenberg, Germany). The excitation filter was set to 360 nm and the emission filters were set to 420 and 520 nm. Fluorescence intensities at 420 nm (I_{420}) and 520 nm (I_{520}) of three samples were averaged and used to calculate the generalized polarization (GP) after subtraction of buffer background (25):

$$GP = \frac{I_{420} - I_{520}}{I_{420} + I_{520}} \quad (\text{Eq. 2})$$

Mg²⁺ binding triggers rearrangement of the IM30 ring

Acrylamide quenching

1.6 μM IM30 in absence or presence of 15 mM MgCl_2 , respectively, were incubated with 0 to 400 mM of freshly prepared acrylamide (Sigma-Aldrich) for 30 min at room temperature (20 mM HEPES, pH 7.6). Trp fluorescence was measured at 25 °C from 310 to 370 nm (slit width 3 nm) upon excitation at 300 nm (slit width 3 nm), to minimize the influence of Tyr absorbance. The fluorescence intensities at 333 nm of three individual measurements were averaged and corrected for inner filter effects by correlating the spectra to the intensities of the water Raman peak under the same conditions without addition of protein. The Stern–Volmer equation,

$$\frac{F_{Q0}}{F_Q} - 1 = K_{SV} * [Q] \quad (\text{Eq. 3})$$

was used to determine the Stern–Volmer constant (K_{SV}) from linear regression of the data. Here, F_Q is the measured fluorescence intensity at 333 nm, F_{Q0} is the intensity in absence of quencher, and $[Q]$ is the acrylamide concentration (34).

Förster resonance energy transfer measurements

For FRET measurements, IM30-CFP and IM30-Venus (1 μM each) were mixed and incubated for ~2 h at room temperature with the indicated Mg^{2+} concentrations. The donor (CFP) was excited at 420 nm (slit width 2 nm) and fluorescence emission was recorded from 440 to 700 nm (slit width 2 nm). As reference for the actual concentration of acceptor for each sample, a spectrum between 517 to 700 nm was recorded (slit 1 nm) after acceptor excitation (510 nm, slit 1 nm). As a measure of FRET efficiency, the ratiometric FRET efficiency E_{rat} was calculated using the equation

$$E_{\text{rat}} = \frac{1}{1 + \frac{I_D}{I_A}} \quad (\text{Eq. 4})$$

where I_D is the fluorescence intensity of the donor emission at 475 nm and I_A is the fluorescence intensity of the acceptor emission at 528 nm, both after donor excitation. E_{rat} is suitable for comparing the relative ratio between donor and acceptor peak in a qualitative manner. Kinetics of changes in FRET were measured in presence or absence of 7.5 mM MgCl_2 . Samples were prepared as described above and spectra were recorded at different time points. To estimate the E_{rat} level of rings composed of a 1:1 ratio of monomers tagged with CFP and Venus, respectively, cells expressing either CFP- or Venus-labeled IM30 were broken and cell suspensions were mixed prior to purification following the standard procedure described above. As observed recently (36), IM30 tetramers are purified with this procedure, and the tetramers reassembly to IM30 rings directly after purification, resulting in mixed CFP/Venus-labeled rings. The ratio of the two constructs was determined via SDS-PAGE. E_{rat} was determined as described above.

Static light scattering

Static light scattering was used to follow particle size changes of IM30 in presence of increasing Mg^{2+} concentrations. 1.6 μM

IM30 was incubated for 15 min at room temperature in presence of increasing Mg^{2+} concentrations in 20 mM HEPES buffer, pH 7.6. The samples were excited at 600 nm (slit width 5 nm) and emission spectra were recorded from 200 to 400 nm (slit width 5 nm). The intensities of the Rayleigh scattering peaks of at least three samples were measured at the second-order wavelength (300 nm) and were plotted against the Mg^{2+} concentrations.

Isothermal titration calorimetry

ITC experiments were performed using a MicroCal VP-ITC microcalorimetry system (Malvern Panalytical, Worcester-shire, UK). The sample cell contained 0–50 mM MgCl_2 solutions in 20 mM HEPES buffer, pH 7.6. The syringe was loaded with 20 μM IM30 in 20 mM HEPES buffer, pH 7.6. All solutions were degassed thoroughly under vacuum prior to the measurements. Three injections of 20 μl per Mg^{2+} concentration were carried out at 20 °C and changes in the heating rate were measured (reference heat rate 20 $\mu\text{cal/s}$). The origin-based MicroCal ITC software was used to automatically calculate the enthalpy change by integrating the heat rate peaks. The enthalpy change of three injections was averaged, assuming a negligible change in the molar ratio between ligand and protein because of the high dilution of the protein. The data were corrected for heats of dilution of Mg^{2+} by subtracting enthalpy changes of control experiments that were done with buffer instead of protein solutions and by subtracting the value for adding 0 mM Mg^{2+} from all data points.

A hyperbolic binding function was fitted to the data in the concentration range of 0 to 15 mM Mg^{2+} to determine the dissociation constant (K_d) by the nonlinear least square algorithm implemented in OriginPro 8.6.0 (54, 55). Because of the low affinity of the binding process, the concentration of Mg^{2+} was significantly higher than the protein concentration, allowing use of the simple hyperbolic binding function.

Transmission EM

6.3 μM IM30 was incubated for 30 min in presence of 15 mM MgCl_2 in 20 mM HEPES buffer, pH 7.6. The control sample contained the same amount of protein from the same stock solution and was prepared under the same conditions without MgCl_2 . The samples were processed and imaged as described previously (49).

Fourier transform IR spectroscopy

First, a gold layer was deposited on the surface of a silicon ATR crystal by etching the silicon with HF and by reduction of AuCl_4^- as described previously (56). Prior to the deposition of the gold film, the ATR crystal was polished with 0.3 μm alumina, rinsed with copious amounts of Millipore water, acetone, and water again. The crystal was then dried under an argon stream and immersed in 40% NH_4F (w/v) for 1 min, rinsed, and dried again. It was then heated at 65 °C for 10 min together with the plating solution. This solution was a 1:1:1 mix (v/v/v) of (a) 15 mM NaAuCl_4 ; (b) 150 mM Na_2SO_3 , 50 mM $\text{Na}_2\text{S}_2\text{O}_3$, and 50 mM NH_4Cl ; and (c) HF 2% (w/v) (total volume, 1 ml). Once the plating temperature was reached, the prism was covered with the solution for 40 s, and the reaction was stopped by

washing the plating solution off with water, followed by drying with a stream of argon. The resulting gold film was then tested for electrical conductance with a multimeter (the typical electric resistance of the layer as measured from one corner to another of the crystal should be around 15 Ω for a thickness of 50 nm).

The experimental procedure for the nickel-nitrilotriacetic acid *S*-adenosylmethionine (Fig. S4, B–E) was adapted from (57, 58). First, the gold-modified silicon ATR crystal was covered with 1 mg/ml of 3,3'-dithiodipropionic acid di(N-hydroxysuccinimide ester) (DTSP) (Sigma-Aldrich) in dry DMSO and the monolayer was allowed to self-assemble for 1 h. The excess DTSP was then washed away with dry DMSO and the crystal was dried under an argon stream. Afterward, it was covered with 100 mM Na α' ,Na α'' -bis(carboxymethyl)-L-lysine (Sigma-Aldrich) in 0.5 M K₂CO₃ at pH 9.8 for 3 h and then rinsed with water. Finally, the surface was incubated in 50 mM Ni(ClO₄)₂ for 1 h before being washed one last time with water. For immobilization of the protein, 5 μ l of 21.2 μ M IM30 in 20 mM HEPES, pH 7.6, were deposited on the modified gold surface for 1 h.

A configuration allowing the simultaneous acquisition of FTIR spectra in the ATR mode with perfusion of solutions with given composition was used. As a multireflection ATR unit, we used silicon crystal with 3 mm surface diameter. All experiments were carried out with a Bruker Vertex 70 FTIR spectrometer (Gloab source, KBr Beamsplitter, LN-MCT detector) at 8 mm aperture and 40 kHz scanner velocity. The measurements were carried out at \sim 7 °C. Solutions were kept on ice prior to use. The pump speed was kept constant at a flow rate of 0.2 ml/min. Before each perfusion step, the input tube was carefully washed with water and buffer.

For recording IM30 differences spectra, MgCl₂ was dissolved in 20 mM HEPES, pH 7.6, to a final concentration of 10 and 90 mM. A second perfusion solution of the same composition but without MgCl₂ at a given pH value was also used. Before measuring perfusion-induced difference spectra, the system was perfused first with HEPES buffer without MgCl₂ for 30 min to equilibrate the system. A background spectrum was then recorded and the perfusion was changed to HEPES buffer containing MgCl₂. After a delay of 20 min for equilibration, the Mg²⁺ minus Mg²⁺-free difference spectra were recorded. Subsequently, a new background was recorded, and the solution was changed back to the solution without Mg²⁺. The equilibration time was again 20 min and Mg²⁺-free minus Mg²⁺ spectra were obtained. The procedure described was repeated five times, and the difference spectra were averaged. Baseline correction and smoothing were done, where necessary. Full reversibility is indicated by a symmetrical shape of the two spectra obtained.

The secondary structure was determined on the basis of deconvolution of the amide I signal of the dried films in the presence and absence of Mg²⁺. First, the wave number of each component was determined from the second derivative of the individual spectrum and Gaussian curves were fitted to each absorption spectrum (Origin 8.5 software) whereas the identified position was kept constant during the first fitting. Then, a consecutive optimization of amplitudes, band positions and the

half-width of the individual bands were performed (Fig. S4, F and G). The individual amide I band components were obtained at 1621, 1654, 1687, and 1699 cm⁻¹ and have been assigned to the secondary structure elements as follows: α -helices and unordered structures (1660–1640 cm⁻¹), anti-parallel β -sheet (two bands in 1621 and 1699 cm⁻¹), and β -turns (1687 cm⁻¹), on the basis of a large body of experimental data (59). Because of the fitting procedure, the error is \pm 1%.

Circular dichroism spectroscopy

CD was measured using a Jasco-815 CD spectrometer (Jasco Inc., Easton, MD). Spectra ranging from 200 to 250 nm were recorded at 20 °C with a scan rate of 100 nm/min, 1-nm steps and 1-s data integration time. For each sample, three spectra were averaged and smoothed by the Jasco software package (Savitzky–Golay filter), if necessary. All spectra were converted to molar ellipticity (60).

The helix–interaction ratio (coiled coil ratio) of IM30 in presence and absence of Mg²⁺ was calculated as the ratio of molar ellipticity at 222 nm and 208 nm (32). For this calculation, the ratio determined from at least six independent samples was averaged. To test the statistical significance of the differences, we performed one-way analysis of variance (ANOVA) (OriginPro 8.6.0), testing for the population means of the 222/208 nm ratios with *p* levels of 0.05, 0.01, and 0.001.

The stability of IM30 was determined by incubating 3.2 μ M IM30 with increasing concentrations of urea (0–6.5 M) in 10 mM sodium phosphate buffer, pH 7.6, for 30 min at room temperature. Protein denaturation was followed in presence of 0–15 mM Mg²⁺. For protein renaturation, the urea concentration was lowered stepwise by dialysis for 90 min and spectra were recorded at each step. Three independent measurements were averaged.

The transition point of the denaturation curve ($D_{1/2}$) was calculated by a least square nonlinear fit of the following Boltzmann equation:

$$f_D = \frac{y_N - y_D}{1 + e^{(x - D_{1/2})/dx}} + y_D \quad (\text{Eq. 5})$$

Here, y_N is the molar ellipticity at 222 nm in the native state and y_D the molar ellipticity at 222 nm in the denatured state. f_D is the fraction of denatured protein and x the concentration of urea.

Trypsin digestion of IM30

2.5 μ M IM30 in presence and absence of 10 mM Mg²⁺ was incubated with 0.01 mg/ml trypsin (bovine pancreas, 5000 USP/mg, Sigma-Aldrich) at 37 °C for 0 to 60 min. The reaction was stopped immediately by adding 5 \times SDS loading buffer (containing 250 mM Tris, 10% SDS (w/v), 0.2% bromophenol blue (w/v), 50% glycerol (w/v), 500 mM DTT) and by heating to 95 °C for 3 min. The samples were analyzed on a SDS-PAGE gel and via immunoblotting using an antibody directed against the IM30 C-terminal domain (rabbit) (Gramsch Laboratories, Schwabhausen, Germany) and a peroxidase coupled anti-rabbit secondary antibody (Sigma-Aldrich) with subsequent visual-

ization by the GE Healthcare Amersham ECLTM Prime Western Blotting Detection Reagent kit (Thermo Fisher Scientific).

As a control for a potential interaction of trypsin with Mg²⁺, the trypsin activity was determined using an N_α-benzoyl-L-arginine ethyl ester (BAEE) assay (Acros Organics, Geel, Belgium) in presence and absence of Mg²⁺ (61). The trypsin activity of three samples was averaged. The activity of trypsin in absence of Mg²⁺ was set as 100%. Activities of trypsin in presence of salts were calculated relative to this.

Size exclusion chromatography

To confirm formation of high-molecular-weight particles of IM30-CFP and IM30-Venus, 350 or 250 μg protein, respectively, were loaded onto a Superdex 200 16/600 column at 4 °C using an Äkta Explorer system (GE Healthcare) at a flow rate of 0.5 ml/min. For calibration, the following proteins of the molecular weight marker kit (Sigma Aldrich) were used: RNase A (13.7 kDa), carbonic anhydrase (29 kDa), BSA (66 kDa), β-amylase (200 kDa), and apoferritin (443 kDa).

Author contributions—J. H., B. J., N. G., N. H., K. R., and W. G. investigation; J. H. and P. H. methodology; J. H., B. J., P. H., and D. S. writing-original draft; B. J., N. H., P. H., and D. S. conceptualization; B. J., N. G., N. H., K. R., W. G., P. H., and D. S. formal analysis; B. J., N. H., and W. G. validation; N. H., J. M., P. H., and D. S. writing-review and editing; J. M. and D. S. resources; J. M. and D. S. funding acquisition; D. S. supervision; D. S. project administration.

References

- Adam, Z., Charuvi, D., Tsabari, O., Knopf, R. R., and Reich, Z. (2011) Biogenesis of thylakoid networks in angiosperms: Knowns and unknowns. *Plant Mol. Biol.* **76**, 221–234 [CrossRef Medline](#)
- Barthel, S., Bernát, G., Seidel, T., Rupprecht, E., Kahmann, U., and Schneider, D. (2013) Thylakoid membrane maturation and PSII activation are linked in greening *Synechocystis* sp. PCC 6803 cells. *Plant Physiol.* **163**, 1037–1046 [CrossRef Medline](#)
- Frain, K. M., Gangl, D., Jones, A., Zedler, J. A., and Robinson, C. (2016) Protein translocation and thylakoid biogenesis in cyanobacteria. *Biochim. Biophys. Acta* **1857**, 266–273 [CrossRef Medline](#)
- Liberton, M., Page, L. E., O'Dell, W. B., O'Neill, H., Mamontov, E., Urban, V. S., and Pakrasi, H. B. (2013) Organization and flexibility of cyanobacterial thylakoid membranes examined by neutron scattering. *J. Biol. Chem.* **288**, 3632–3640 [CrossRef Medline](#)
- Li, H. M., Kaneko, Y., and Keegstra, K. (1994) Molecular cloning of a chloroplastic protein associated with both the envelope and thylakoid membranes. *Plant Mol. Biol.* **25**, 619–632 [CrossRef Medline](#)
- Westphal, S., Heins, L., Soll, J., and Vothknecht, U. C. (2001) Vipp1 deletion mutant of *Synechocystis*: A connection between bacterial phage shock and thylakoid biogenesis? *Proc. Natl. Acad. Sci. U.S.A.* **98**, 4243–4248 [CrossRef Medline](#)
- Brissette, J. L., Russel, M., Weiner, L., and Model, P. (1990) Phage shock protein, a stress protein of *Escherichia coli*. *Proc. Natl. Acad. Sci. U.S.A.* **87**, 862–866 [CrossRef Medline](#)
- Brissette, J. L., Weiner, L., Ripmaster, T. L., and Model, P. (1991) Characterization and sequence of the *Escherichia coli* stress-induced psp operon. *J. Mol. Biol.* **220**, 35–48 [CrossRef Medline](#)
- Kroll, D., Meierhoff, K., Bechtold, N., Kinoshita, M., Westphal, S., Vothknecht, U. C., Soll, J., and Westhoff, P. (2001) VIPP1, a nuclear gene of *Arabidopsis thaliana* essential for thylakoid membrane formation. *Proc. Natl. Acad. Sci. U.S.A.* **98**, 4238–4242 [CrossRef Medline](#)
- Hennig, R., Heidrich, J., Saur, M., Schmäser, L., Roeters, S. J., Hellmann, N., Woutersen, S., Bonn, M., Weidner, T., Markl, J., and Schneider, D. (2015) IM30 triggers membrane fusion in cyanobacteria and chloroplasts. *Nat. Commun.* **6**, 7018 [CrossRef Medline](#)
- Fuhrmann, E., Bultema, J. B., Kahmann, U., Rupprecht, E., Boekema, E. J., and Schneider, D. (2009) The vesicle-inducing protein 1 from *Synechocystis* sp. PCC 6803 organizes into diverse higher-ordered ring structures. *Mol. Biol. Cell* **20**, 4620–4628 [CrossRef Medline](#)
- Bultema, J. B., Fuhrmann, E., Boekema, E. J., and Schneider, D. (2010) Vipp1 and PspA: Related but not twins. *Commun. Integrative Biol.* **3**, 162–165 [CrossRef](#)
- Hankamer, B. D., Elderkin, S. L., Buck, M., and Nield, J. (2004) Organization of the AAA(+) adaptor protein PspA is an oligomeric ring. *J. Biol. Chem.* **279**, 8862–8866 [CrossRef Medline](#)
- Otters, S., Braun, P., Hubner, J., Wanner, G., Vothknecht, U. C., and Chigri, F. (2013) The first alpha-helical domain of the vesicle-inducing protein in plastids 1 promotes oligomerization and lipid binding. *Planta* **237**, 529–540 [CrossRef Medline](#)
- Aseeva, E., Ossenbühl, F., Eichacker, L. A., Wanner, G., Soll, J., and Vothknecht, U. C. (2004) Complex formation of Vipp1 depends on its alpha-helical PspA-like domain. *J. Biol. Chem.* **279**, 35535–35541 [CrossRef Medline](#)
- Saur, M., Hennig, R., Young, P., Rusitzka, K., Hellmann, N., Heidrich, J., Morgner, N., Markl, J., and Schneider, D. (2017) A Janus-faced IM30 ring involved in thylakoid membrane fusion is assembled from IM30 tetramers. *Structure* **25**, 1380–1390.e5 [CrossRef Medline](#)
- Vothknecht, U. C., Otters, S., Hennig, R., and Schneider, D. (2012) Vipp1: A very important protein in plastids?!. *J. Exp. Bot.* **63**, 1699–1712 [CrossRef Medline](#)
- Fuhrmann, E., Gathmann, S., Rupprecht, E., Golecki, J., and Schneider, D. (2009) Thylakoid membrane reduction affects the photosystem stoichiometry in the cyanobacterium *Synechocystis* sp. PCC 6803. *Plant Physiol.* **149**, 735–744 [CrossRef Medline](#)
- Heidrich, J., Thurotte, A., and Schneider, D. (2017) Specific interaction of IM30/Vipp1 with cyanobacterial and chloroplast membranes results in membrane remodeling and eventually in membrane fusion. *Biochim. Biophys. Acta* **1859**, 537–549 [CrossRef Medline](#)
- Shaul, O. (2002) Magnesium transport and function in plants: The tip of the iceberg. *Biomaterials* **15**, 309–323 [Medline](#)
- Lin, D. C., and Nobel, P. S. (1971) Control of photosynthesis by Mg²⁺. *Arch. Biochem. Biophys.* **145**, 622–632 [CrossRef Medline](#)
- Hind, G., Nakatani, H. Y., and Izawa, S. (1974) Light-dependent redistribution of ions in suspensions of chloroplast thylakoid membranes. *Proc. Natl. Acad. Sci. U.S.A.* **71**, 1484–1488 [CrossRef Medline](#)
- Scholnick, S., and Keren, N. (2006) Metal homeostasis in cyanobacteria and chloroplasts. Balancing benefits and risks to the photosynthetic apparatus. *Plant Physiol.* **141**, 805–810 [CrossRef Medline](#)
- Martín-Molina, A., Rodríguez-Beas, C., and Faraudo, J. (2012) Effect of calcium and magnesium on phosphatidylserine membranes: Experiments and all-atomic simulations. *Biophys. J.* **102**, 2095–2103 [CrossRef Medline](#)
- Parasassi, T., De Stasio, G., d'Ubaldo, A., and Gratton, E. (1990) Phase fluctuation in phospholipid membranes revealed by Laurdan fluorescence. *Biophys. J.* **57**, 1179–1186 [CrossRef Medline](#)
- Baker, B. M., and Murphy, K. P. (1996) Evaluation of linked protonation effects in protein binding reactions using isothermal titration calorimetry. *Biophys. J.* **71**, 2049–2055 [CrossRef Medline](#)
- Gasymov, O. K., and Glasgow, B. J. (2007) ANS fluorescence: Potential to augment the identification of the external binding sites of proteins. *Biochim. Biophys. Acta* **1774**, 403–411 [CrossRef Medline](#)
- LaPorte, D. C., Wierman, B. M., and Storm, D. R. (2002) Calcium-induced exposure of a hydrophobic surface on calmodulin. *Biochemistry* **19**, 3814–3819
- Venjaminov, S. Yu., and Kalnin, N. N. (1990) Quantitative IR spectrophotometry of peptide compounds in water (H₂O) solutions. I. Spectral parameters of amino acid residue absorption bands. *Biopolymers* **30**, 1243–1257 [CrossRef Medline](#)
- Arrondo, J. L. R., Muga, A., Castresana, J., and Goñi, F. M. (1993) Quantitative studies of the structure of proteins in solution by Fourier-

- transform infrared spectroscopy. *Progr. Biophys. Mol. Biol.* **59**, 23–56 [CrossRef](#)
31. Myers, J. K., Pace, C. N., and Scholtz, J. M. (1995) Denaturant m values and heat capacity changes: Relation to changes in accessible surface areas of protein unfolding. *Protein Sci.* **4**, 2138–2148 [CrossRef](#) [Medline](#)
32. Lau, S. Y., Taneja, A. K., and Hodges, R. S. (1984) Synthesis of a model protein of defined secondary and quaternary structure. Effect of chain length on the stabilization and formation of two-stranded α -helical coiled-coils. *J. Biol. Chem.* **259**, 13253–13261 [Medline](#)
33. Osadnik, H., Schöpfel, M., Heidrich, E., Mehner, D., Lilie, H., Parthier, C., Risselada, H. J., Grubmüller, H., Stubbs, M. T., and Brüser, T. (2015) PspF-binding domain PspA1–144 and the PspA.F complex: New insights into the coiled-coil-dependent regulation of AAA+ proteins. *Mol. Microbiol.* **98**, 743–759 [CrossRef](#) [Medline](#)
34. Strambini, G. B., and Gonnelli, M. (2010) Fluorescence quenching of buried Trp residues by acrylamide does not require penetration of the protein fold. *J. Phys. Chem. B* **114**, 1089–1093 [CrossRef](#) [Medline](#)
35. Bryan, S. J., Burroughs, N. J., Shevela, D., Yu, J., Rupprecht, E., Liu, L. N., Mastroianni, G., Xue, Q., Llorente-Garcia, I., Leake, M. C., Eichacker, L. A., Schneider, D., Nixon, P. J., and Mullineaux, C. W. (2014) Localisation and interactions of the Vipp1 protein in cyanobacteria. *Mol. Microbiol.* **94**, 1179–1195 [CrossRef](#) [Medline](#)
36. Heidrich, J., Wulf, V., Hennig, R., Saur, M., Markl, J., Sönnichsen, C., and Schneider, D. (2016) Organization into higher ordered ring structures counteracts membrane binding of IM30, a protein associated with inner membranes in chloroplasts and cyanobacteria. *J. Biol. Chem.* **291**, 14954–14962 [CrossRef](#) [Medline](#)
37. Black, C. B., Huang, H. W., and Cowan, J. A. (1994) Biological coordination chemistry of magnesium, sodium, and potassium ions. Protein and nucleotide binding sites. *Coordination Chem. Rev.* **135–136**, 165–202
38. Ohki, S., Ikura, M., and Zhang, M. (1997) Identification of Mg²⁺-binding sites and the role of Mg²⁺ on target recognition by calmodulin. *Biochemistry* **36**, 4309–4316 [CrossRef](#) [Medline](#)
39. Sissi, C., and Palumbo, M. (2009) Effects of magnesium and related divalent metal ions in topoisomerase structure and function. *Nucleic Acids Res.* **37**, 702–711 [CrossRef](#) [Medline](#)
40. Bellsolle, L., Prieto, J., Serrano, L., and Coll, M. (1994) Magnesium binding to the bacterial chemotaxis protein CheY results in large conformational changes involving its functional surface. *J. Mol. Biol.* **238**, 489–495 [CrossRef](#) [Medline](#)
41. Chin-Sang, I. D., and Spence, A. M. (1996) *Caenorhabditis elegans* sex-determining protein FEM-2 is a protein phosphatase that promotes male development and interacts directly with FEM-3. *Genes Dev.* **10**, 2314–2325 [CrossRef](#) [Medline](#)
42. Portis, A. R. (1992) Regulation of ribulose 1,5-bisphosphate carboxylase/oxygenase activity. *Ann. Rev. Plant Physiol. Plant Mol. Biol.* **43**, 415–437 [CrossRef](#)
43. Portis, A. R., Jr., Chon, C. J., Mosbach, A., and Heldt, H. W. (1977) Fructose and sedoheptulosebisphosphatase. The sites of a possible control of CO₂ fixation by light dependent changes of the stromal Mg²⁺ concentration. *Biochim. Biophys. Acta* **461**, 313–325 [CrossRef](#) [Medline](#)
44. Shaul, O. (2002) Magnesium transport and function in plants: The tip of the iceberg. *BioMetals* **15**, 307–321 [CrossRef](#)
45. Portis, A. R., Jr., and Heldt, H. W. (1976) Light-dependent changes of the Mg²⁺ concentration in the stroma in relation to the Mg²⁺ dependency of CO₂ fixation in intact chloroplasts. *Biochim. Biophys. Acta* **449**, 434–436 [CrossRef](#) [Medline](#)
46. Ishijima, S., Uchibori, A., Takagi, H., Maki, R., and Ohnishi, M. (2003) Light-induced increase in free Mg²⁺ concentration in spinach chloroplasts: Measurement of free Mg²⁺ by using a fluorescent probe and necessity of stromal alkalization. *Arch. Biochem. Biophys.* **412**, 126–132 [CrossRef](#) [Medline](#)
47. Portis, A. R. (1981) Evidence of a low stromal Mg(2+) concentration in intact chloroplasts in the dark: I. Studies with the ionophore A23187. *Plant Physiol.* **67**, 985–989 [CrossRef](#) [Medline](#)
48. Patterson, G. H., Piston, D. W., and Barisas, B. G. (2000) Forster distances between green fluorescent protein pairs. *Anal. Biochem.* **284**, 438–440 [CrossRef](#) [Medline](#)
49. Hennig, R., West, A., Debus, M., Saur, M., Markl, J., Sachs, J. N., and Schneider, D. (2017) The IM30/Vipp1 C-terminus associates with the lipid bilayer and modulates membrane fusion. *Biochim. Biophys. Acta* **1858**, 126–136 [CrossRef](#) [Medline](#)
50. Bisicchia, P., Botella, E., and Devine, K. M. (2010) Suite of novel vectors for ectopic insertion of GFP, CFP and YFP transcriptional fusions in single copy at the amyE and bglS loci in *Bacillus subtilis*. *Plasmid* **64**, 143–149 [CrossRef](#) [Medline](#)
51. Nagai, T., Ibata, K., Park, E. S., Kubota, M., Mikoshiba, K., and Miyawaki, A. (2002) A variant of yellow fluorescent protein with fast and efficient maturation for cell-biological applications. *Nat. Biotechnol.* **20**, 87–90 [CrossRef](#) [Medline](#)
52. Migneault, I., Dartiguenave, C., Bertrand, M. J., and Waldron, K. C. (2004) Glutaraldehyde: Behavior in aqueous solution, reaction with proteins, and application to enzyme crosslinking. *BioTechniques* **37**, 790–796, 798–802 [Medline](#)
53. Hemaprabha, E. (2012) Chemical crosslinking of proteins: A review. *J. Pharmaceutical Scientific Innovation* **1**, 22–26
54. Xie, D., Gulnik, S., Collins, L., Gustchina, E., Suvorov, L., and Erickson, J. W. (1997) Dissection of the pH dependence of inhibitor binding energetics for an aspartic protease: Direct measurement of the protonation states of the catalytic aspartic acid residues. *Biochemistry* **36**, 16166–16172 [CrossRef](#) [Medline](#)
55. Velazquez-Campoy, A., Ohtaka, H., Nezami, A., Muzammil, S., and Freire, E. (2004) Isothermal titration calorimetry. *Curr. Protoc. Cell Biol.* Chapter 17:Unit 17.8 [CrossRef](#) [Medline](#)
56. Grytsyk, N., Sugihara, J., Kaback, H. R., and Hellwig, P. (2017) pKa of Glu325 in LacY. *Proc. Natl. Acad. Sci. U.S.A.* **114**, 1530–1535 [CrossRef](#) [Medline](#)
57. Kriegl, S., Uchida, T., Osawa, M., Friedrich, T., and Hellwig, P. (2014) Biomimetic environment to study *E. coli* complex I through surface-enhanced IR absorption spectroscopy. *Biochemistry* **53**, 6340–6347 [CrossRef](#) [Medline](#)
58. Ataka, K., Giess, F., Knoll, W., Naumann, R., Haber-Pohlmeier, S., Richter, B., and Heberle, J. (2004) Oriented attachment and membrane reconstitution of His-tagged cytochrome c oxidase to a gold electrode: In situ monitoring by surface-enhanced infrared absorption spectroscopy. *J. Am. Chem. Soc.* **126**, 16199–16206 [CrossRef](#) [Medline](#)
59. Goormaghtigh, E., Cabiaux, V., and Ruyschaert, J. (1994) Determination of soluble and membrane protein structure by Fourier transform infrared spectroscopy. III. Secondary structures. *Subcell Biochem.* **23**, 405–450 [CrossRef](#) [Medline](#)
60. Myers, J. K., Pace, C. N., and Scholtz, J. M. (1997) Helix propensities are identical in proteins and peptides. *Biochemistry* **36**, 10923–10929 [CrossRef](#)
61. Fritz, H., and Bergmeyer, H. U. (eds) (1984) *Methods of Enzymatic Analysis: Hans Ulrich Bergmeyer*, Verlag Chemie, Weinheim